Electrostatic interactions vs. second order Jahn-Teller distortion as the source of structural diversity in Li 3 MO 4 compounds (M = Ru, Nb, Sb and Ta)

Quentin Jacquet, Gwenaëlle Rousse, Antonella Iadecola, Matthieu Saubanère, Marie-Liesse Doublet, Jean-Marie Tarascon

Electrostatic interactions vs. second order Jahn-Teller distortion as the source of structural diversity in Li_3MO_4 compounds (M = Ru, Nb, Sb and Ta).

Quentin Jacquet[a,b,c], Gwenaëlle Rousse[a,b,c], Antonella Iadecola[c], Matthieu Saubanère[c,d], Marie-Liesse Doublet[c,d], Jean-Marie Tarascon[a,b,c].

[a] Collège de France, Chaire de Chimie du Solide et de l'Energie, UMR 8260, 11 place Marcelin Berthelot, 75231 Paris CEDEX 05, France

[b] Sorbonne Universités – UPMC Univ. Paris 06, 4 place Jussieu, F-75005 Paris, France

[c] Réseau sur le Stockage Electrochimique de l'Energie (RS2E), FR CNRS 3459 – France

[d] Institut Charles Gerhardt, CNRS UMR 5253, Université Montpellier, Place E. Bataillon, 34 095 Montpellier, France

Abstract:

With the advent of layered rocksalt oxides showing anionic redox activity towards Li, there has been an increased focus on designing new rocksalt structures and more particularly, compounds pertaining to the Li_3MO_4 family. The structural richness of this family is nested in its ability to host many different cations, leading to the formation of superstructure patterns whose predictability is still limited. Thus, there is a need to understand the formation of such superstructures, as cationic arrangements have a crucial effect on their physical properties. Herein we propose a combined experimental and theoretical approach to understand the interactions governing cation ordering in binary systems of general composition given by $Li_3M_yM'_{1-y}O_4$ (M and M' being Ru, Nb, Sb, and Ta). Through complementary X-ray diffraction and X-ray absorption spectroscopy techniques, we reveal a solid-solution behavior for the $Li_3Ru_ySb_{1-y}O_4$ system, as opposed to $Li_3Sb_yNb_{1-y}O_4$ that enlists four rocksalt structures with different cation orderings. We use DFT calculations to rationalize such a structural diversity and find that it is controlled by a delicate balance between electrostatic interactions and charge transfer due to a second order Jahn-Teller distortion. This insight provides a new viewpoint for understanding cationic arrangements in rocksalt structures, and guidelines to design novel phases for applications such as Li-ion batteries or ionic conductors.

Introduction:

Oxides have always been a rich playground for solid-state scientists due to their vast chemical compositions, structural diversity, and intriguing electronic properties. The rocksalt type (NaCl) structure is one the most common structural families, and many of its representatives have been studied in different fields, for example magnetism as for β–Li_2IrO_3 [1] or Ag_3RuO_4 [2], dielectrics like Li_2TiO_3 or Li_3NbO_4 derivatives[3,4], and electrochemical energy storage via Li-ion or Na-ion batteries.[5, 6]

Within a rocksalt structure of general composition MO with M being the cation, the atomic arrangement presents three important features: i) all cations are octahedrally coordinated by anions and so are the anions by the cations, ii) anions are close-packed (FCC stacking) and all octahedral interstices are occupied with cations, and iii) MO_6 octahedra are connected by their edges. The richness of this structural family is nested in its ability to host different cations which lead to distortions of the cubic structure, and also generate superstructure patterns. For example, NiO forms a simple rocksalt structure whereas $Li_{0.5}Ni_{0.5}O$ (or $LiNiO_2$) crystallizes in a *layered* rocksalt structure, in which Ni and Li segregate to form alternate layers of Ni and layers of Li.[7] In light of the different cation orderings [8, 9, 10], together with a diversity of chemical elements that the structure can accommodate, oxides with a rocksalt structure constitute a vast chemical playground for materials design.

Over the years, guidelines have been established to predict the formation of rocksalt structures and their cation ordering. First, from a geometric consideration, ionic radii of the cation (r_M) and of the anion (r_O) should follow the rule: $0.42 \leq r_M/r_O \leq 0.72$ [11]. Second, electro-neutrality around anions should be respected according to Pauling's rule. This means that the charge of an anion *zo* surrounded by *n* cations *i* of charge *zi* is given by $zo = \sum_i \frac{zi}{n}$. When the chemical composition enlists an alkali ion A^+, only specific combinations of cations can fulfill this rule, such as AMO_2 with $OA^+{}_3M^{3+}{}_3$ octahedra $\left(-2 = -3 * \left(\frac{1}{6}\right) - 3 * \left(\frac{3}{6}\right)\right)$, A_2MO_3 with $OA^+{}_4M^{4+}{}_2$ octahedra $\left(-2 = -4 * \left(\frac{1}{6}\right) - 2 * \left(\frac{4}{6}\right)\right.$, or A_5MO_6 with $OA_5{}^+M^{7+}$ octahedra $\left(-2 = -5 * \left(\frac{1}{6}\right) - 1 * \left(\frac{7}{6}\right)\right)$. Third, studying these specific combinations, Brunel *et al.*[12] and Hauck[13] could predict the cation ordering based on the

polarizability of the anion and the ionic radius ratio between the alkali and the transition metal (r_A/r_M). Overall, prediction of cation ordering in rocksalt structures is quite advanced, however some compounds such as A_3MO_4 are still a mystery for solid-state chemists.[8] Indeed, the $A^+_3M^{5+}O_4$ composition cannot fulfill Pauling's rule at first sight, because the charge around oxygen cannot be compensated by a single octahedron of A^+ and M^{5+} cations. To alleviate this issue, oxygen atoms distribute into two crystallographic sites (O1 and O2), leading to two different octahedra: $O1A^+_5M^{5+}$ and $O2A^+_4M^{5+}_2$. This leads to cation orderings that don't follow the classical rules determined by Brunel *et al.* and Hauck. For instance, Nb^{5+}, Ta^{5+}, and Sb^{5+} have similar sizes and crystal chemistries but Li_3NbO_4 [14], Li_3TaO_4 [15], and Li_3SbO_4 [16] crystallize in different rocksalt structures.

Rocksalt Li_3MO_4, with M being a transition metal, recently received a great interest as cathode material for Li-ion batteries. Yabuuchi et al.[17] used Li_3NbO_4 as a host framework for 3d transition metals and reported interesting performances for the $Li_{1.3}Mn_{0.4}Nb_{0.3}O_2$ compound. Perez et al. reported the highest capacity per transition metal for Li_3IrO_4, thanks to the cumulative cationic and anionic redox processes[18]. These findings underline the need to better understand the structure vs. composition relationships with the aim to design new Li_3MO_4 materials. For this, we propose a combined experimental/theoretical approach, which consists in synthetizing new binary phases $Li_3M_xM'_{1-x}O_4$ (M, M' being Ru, Sb, Nb, and Ta), and use these structures as a database to understand the interactions responsible for the cation ordering in Li_3MO_4 systems. The choice of the elements was motivated by their different electronic configurations, i.e. d^0, d^3, and d^{10} respectively for Nb^{5+}, Ru^{5+}, and Sb^{5+}.

Through this study, we unveil the rich crystal chemistry of the $Li_3Sb_yNb_{1-y}O_4$ system which enlists four rocksalt structures with different cation orderings, together with the $Li_3Ru_ySb_{1-y}O_4$ system that forms a solid solution. Such a structural diversity relying on various cation orderings is rationalized using density functional theory (DFT). We report the synthesis of $Li_3Ru_ySb_{1-y}O_4$ and $Li_3Sb_yNb_{1-y}O_4$ and their structural characterization using Synchrotron X-Ray diffraction (SXRD), neutron powder diffraction (NPD), and X-ray absorption spectroscopy (XAS), followed by DFT calculations performed to understand the structural evolution. We show that the structural evolution is controlled by a delicate balance between electrostatic interactions and charge transfer due to the second order Jahn-Teller distortion[19].

Experimental section:

Synthesis

Classical solid-state synthesis from oxide precursors, Nb_2O_5 (Sigma-Aldrich 99.9%), RuO_2 (Alfa Aesar, 99.9%), Sb_2O_3 (Alfa Aesar, 99.998%), Ta_2O_5 (Alfa Aesar, 99.85%), with 10% excess Li_2CO_3 (Sigma Aldrich, 99%), was employed to prepare the $Li_3Ru_ySb_{1-y}O_4$, $Li_3Sb_yNb_{1-y}O_4$, and $Li_3Ta_{0.5}Ru_{0.5}O_4$ compounds with y = 1, 0.7, 0.5, 0.3, and 0. These compositions were chosen so as to get a representative view of the phase diagrams. The reactants were mixed using a mortar and pestle before grinding in a planetary ball-mill using a zirconia set for 1 hour at 600 rpm. Ground powders were fired for 24 h at 900°C in air. Then, the samples were ground, using a mortar and pestle, and fired at 900°C – 1000°C, with the exception of Li_3RuO_4 which suffers from reduction upon prolonged heating. This step was repeated until pure phases were obtained. Heat treatment conditions for each sample are reported in Table S1.

Crystal structure analysis

Synchrotron X-ray diffraction measurements were performed on the 11-BM beamline of the Advanced Photon Source at Argonne National Laboratory, with a wavelength of 0.414167 Å for Li_3NbO_4 and 0.414562 Å for the rest of the compounds. The powder was mixed with an appropriate amount of amorphous silica to limit absorption, and placed in a Kapton capillary (Ø 0.7 mm). Neutron powder diffraction patterns were measured on the D1B powder diffractometer at ILL (Institut Laue-Langevin) with λ = 1.2896 Å. $Li_3Ta_{0.5}Ru_{0.5}O_4$ XRD pattern is collected with a BRUKER D8 Advance diffractometer with Cu Kα radiation ($\lambda_{K\alpha1}$=1.54056 Å, $\lambda_{K\alpha2}$=1.54439 Å) and a Lynxeye XE detector.

Rietveld refinements were performed using the FullProf program[20]. Both neutron and synchrotron data were refined simultaneously with a similar weight for both patterns. Background was taken into account using an interpolation of points. X-ray and neutron absorption were estimated and taken into account in the refinement using a packing fraction of 0.6.

X-ray absorption spectroscopy

XAS measurements at the Ru K-edge, the Sb K-edge, and the Nb K-edge were performed in transmission mode at the ROCK beamline[21] of synchrotron SOLEIL (France). A Si (220) channel-cut quick-XAS monochromator with an energy resolution of 2 eV at 22 keV was used. The intensity of the monochromatic X-ray beam was measured with three consecutive ionization detectors. The

samples were placed between the first and the second ionization chambers. For each measurement, successive spectra were collected at a rate of 2 Hz and averaged out over periods of 5 minutes. The energy calibration was established with simultaneous absorption measurements on a standard (a RuO_2 pellet, a Sb_2O_3 pellet, and a Nb foil for the Ru K-edge, the Sb K-edge, and the Nb K-edge respectively) placed between the second and the third ionization chambers. The data was treated using the Demeter package for energy calibration and normalization[22], and Extended X-ray Absorption Fine Structure (EXAFS) oscillations were fitted using the Artemis software[22]. Fourier transforms of EXAFS oscillations were carried out in the k-range from 4.2 $Å^{-1}$ to 14.9 $Å^{-1}$, from 3.7 $Å^{-1}$ to 14.7 $Å^{-1}$, and from 3.5 $Å^{-1}$ to 13.3 $Å^{-1}$ for the Ru K-edge, the Sb K-edge, and the Nb K-edge, respectively. Fitting was performed in R-range from 1.0 to 2.0 Å using k^2 weight. EXAFS amplitudes and phase-shifts were calculated by FEFF7 starting from the calculated lattice parameters of the structures determined by combined Rietveld refinement of the synchrotron and neutron diffraction patterns. Except the radial distance (R) and the Debye-Waller factor (σ^2), all other parameters were kept constant (CN_i the coordination number, E_0 the difference energy threshold and S_0^2 the amplitude reduction factor) in the conventional least squares modelling using the phase and amplitude factors calculated by FEFF7.

DFT calculations:

Spin-polarized density functional theory (DFT) calculations were performed using the plane-wave density functional theory VASP (Vienna *ab initio* simulation package) code[23, 24] within the generalized gradient approximation of Perdew–Burke–Ernzerhof (PBE) to describe electron exchange and correlation.[25] The rotationally invariant Dudarev method (DFT + U)[26] was used to correct the self-interaction error of conventional DFT for correlated d-electrons. All calculations were performed on a structural model containing 8 formula units, expect for the α–Li_3TaO_4 structure which contained 6 formula units. For structural relaxation, the conjugate gradient method was used until the forces on atoms were below 0.005 eV/Å. Plane-wave cutoff of 600 eV was used for the atomic description. Electrostatic energies and Madelung constants were calculated from formal and Bader charges using a homemade program. For the calculations of Li_3RuO_4, antiferromagnetic configurations were considered as reported in refs. 27 and 28.

Results

Structural determination.

We have explored the ternary Li_3RuO_4-Li_3SbO_4-Li_3NbO_4 phase diagram for which the two end members Li_3RuO_4 and Li_3SbO_4 share the same structure (*P* 2/*c* space group), while Li_3NbO_4 crystallizes in a cubic structure (*I* –4 3 *m*). The study of the y Li_3RuO_4–(1-y) Li_3NbO_4 system for 0 ≤ y ≤ 1 being already reported, [29] we have focused on the synthesis and crystal structure characterization of two other binary systems y Li_3RuO_4–(1-y) Li_3SbO_4 and y Li_3SbO_4–(1-y) Li_3NbO_4 for y = 0, 0.3, 0.5, 0.7, and 1.

All compounds were synthetized using classical solid-state synthesis and pure phase could be obtained in every case, except for $Li_3Sb_{0.5}Nb_{0.5}O_4$ which contains 25% of an impurity phase. For y Li_3RuO_4–(1-y) Li_3SbO_4 and y Li_3SbO_4–(1-y) Li_3NbO_4, the structural determination was performed using various complementary techniques such as SXRD and NPD to obtain accurate information on the atomic positions of heavy (Ru, Sb and Nb) and light (Li and O) elements, respectively. Information on the local environment around each metallic atom, which was not accessible from diffraction techniques owing to the intermixing of Ru, Sb, and Nb within the same crystallographic site, has been obtained by EXAFS analysis at the Ru K-edge, the Sb K-edge, and the Nb K-edge. We were therefore successful in achieving reliable structural models by combining these long-range and short-range probes.

Figure 1 (a-b) shows the SXRD patterns collected for the y Li_3RuO_4–(1-y) Li_3SbO_4 series. Patterns are similar but gradually shifted to lower angles when the Sb content increases, indicating a solid-solution behavior in the $Li_3Ru_ySb_{1-y}O_4$ system for 0 ≤ y ≤ 1. One should note that, for some compositions, certain reflections show very peculiar peak shapes, as shown in

Figure 1 b), indicating a complex microstructure. In the case of Li_3SbO_4, this peculiar peak shape can be reproduced by introducing in the Rietveld refinement three Li_3SbO_4 phases with slightly different cell parameters, as shown in *Figure* 1 c). This distribution of cell parameters may be due to inhomogeneous composition within the sample and/or severe strain effects.

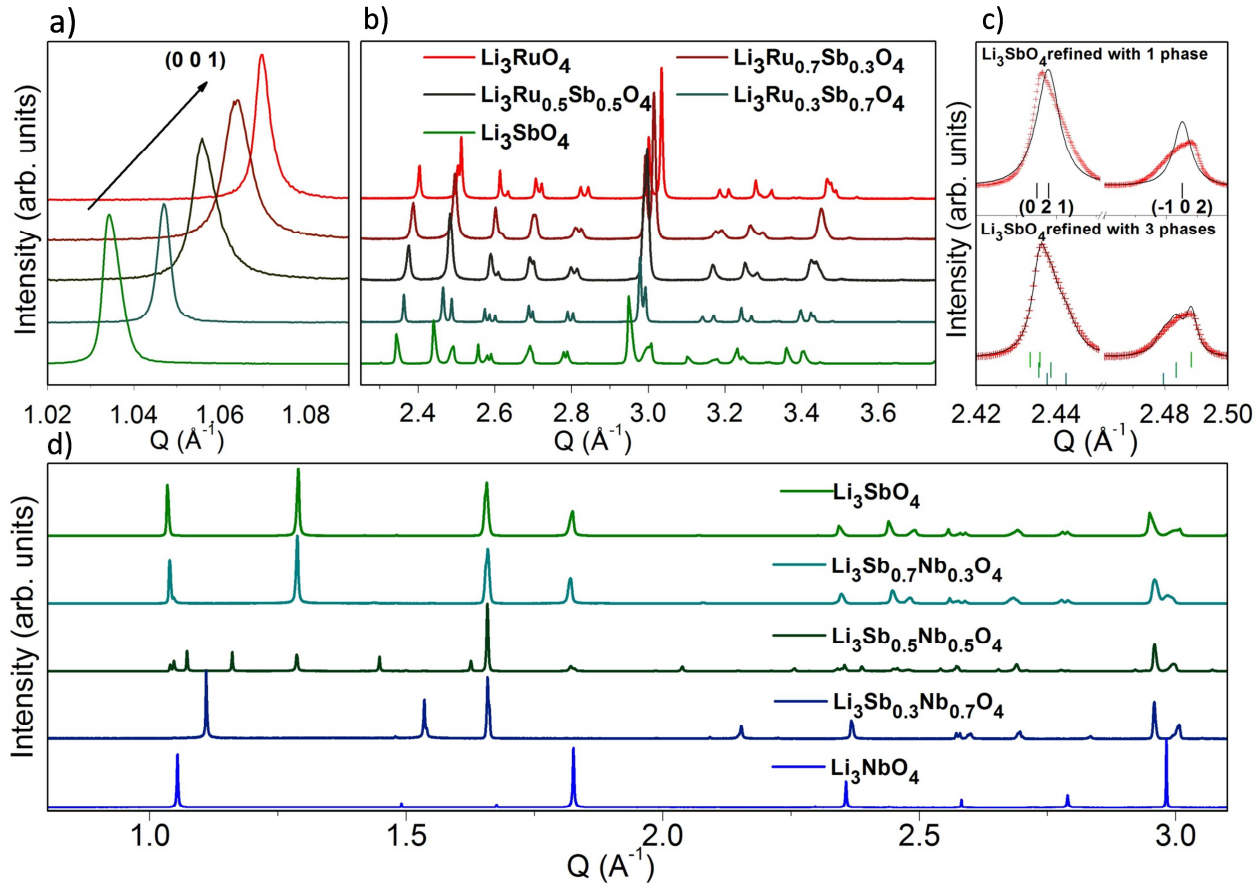

Figure 1

a), and b) Synchrotron X-ray diffraction patterns for the $Li_3Ru_ySb_{1-y}O_4$ samples with y = 1, 0.7, 0.5, 0.3, and 0, at different regions of Q; around the (001) reflection, from 0.8 $Å^{-1}$ to 3.750 $Å^{-1}$, respectively. c) Rietveld refinement of Li_3SbO_4 SXRD pattern using one phase (top) or three phases with the structural model of Li_3SbO_4 but slightly different cell parameters (bottom). The red crosses and black continuous line represent the observed and calculated patterns, respectively. Vertical tick bars are the Bragg positions d) Synchrotron X-ray diffraction patterns for the $Li_3Nb_ySb_{1-y}O_4$ samples with y = 1, 0.7, 0.5, 0.3, and 0.

The SXRD patterns for the y Li_3SbO_4–(1-y) Li_3NbO_4 binary system are shown in

*Figure 1*d. They are quite different depending on the Nb content, nevertheless all could be indexed with already-reported structural models. While $Li_3Sb_{0.7}Nb_{0.3}O_4$ adopts the same structure as Li_3SbO_4, $Li_3Sb_{0.5}Nb_{0.5}O_4$ crystallizes in the α–Li_3TaO_4[30] structure, and $Li_3Sb_{0.3}Nb_{0.7}O_4$ in the β polymorph of Li_3TaO_4[15].

Figure 2 summarizes the evolution of the structure among the binary systems of the ternary $Li_3(Ru,Sb,Nb)O_4$. All structures are rocksalt derivatives and differ in their cation ordering, as emphasized on Figure 2 in which only the transition metal cations are shown. This representation of the metallic framework highlights the Ru, Sb, and Nb connecting modes. For the $Li_3Ru_ySb_{1-y}O_4$ system, the same metallic framework is found over the whole diagram, and consists of zig-zag RuO_6 edge-sharing chains. The $Li_3Sb_yNb_{1-y}O_4$ system is more complex. As the niobium content increases, the arrangement of the M-M bonds transforms from $[MO_6]$ zig-zag chains in $Li_3Sb_yNb_{1-y}O_4$ for y = 1 and 0.75 to $[MO_6]$ "eight"-shaped chains in $Li_3Sb_{0.5}Nb_{0.5}O_4$, then to jagged $[MO_6]$ chains in $Li_3Sb_{0.3}Nb_{0.7}O_4$, and finally to clusters of four $[MO_6]$ in Li_3NbO_4. Together with the structural evolution within the $Li_3Ru_yNb_{1-y}O_4$ system, two main trends for the cation ordering can be seen: i) structures containing Nb^{5+} show a rich diversity, ii) compounds without Nb adopt the same structure.

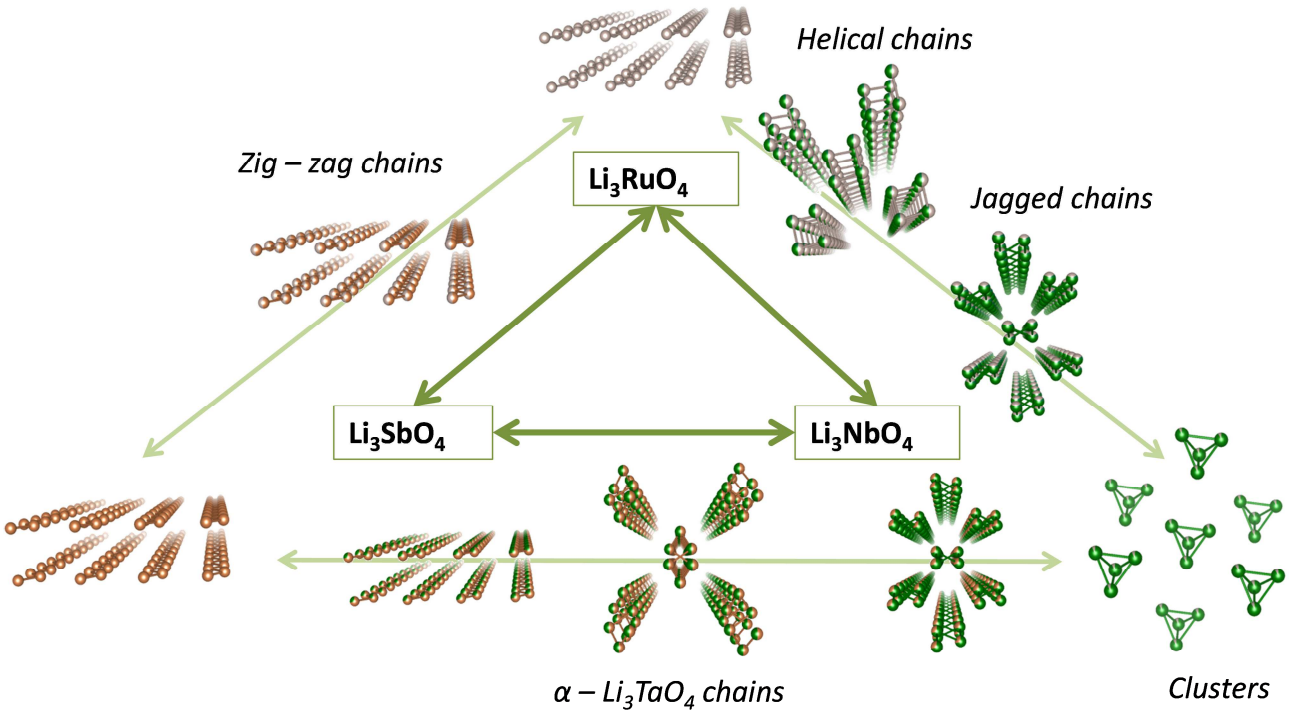

Figure 2

Schematic of the structures of the $Li_3Ru_yNb_{1-y}O_4$, $Li_3Ru_ySb_{1-y}O_4$, and $Li_3Sb_yNb_{1-y}O_4$ for y = 1, 0.7, 0.5, 0.3, and 0. For each composition only the metallic framework, M-M bonds with M = Nb, Sb or Ru, are shown.

To access a better understanding of these structural evolutions, combined Rietveld refinements of SXRD and NPD data were performed on each compound. All compositions of the

$Li_3Ru_ySb_{1-y}O_4$ system (y = 1, 0.7, 0.5, 0.3, and 0) were satisfactorily refined with the structural model of Li_3SbO_4 (*P* 2/*c* space group, zig-zag chains), as can be seen in *Figure 3* a) and Figure S1. Atomic positions are given in Tables S2, S3, and S4. The volume variation with Ru/Sb content follows Vegard's law (Figure 3-c), while cell parameters present a nonlinear evolution with the composition, as can be expected from an anisotropic structure. Note that the synchrotron patterns show both asymmetric and anisotropic broadening of peaks that we have taken into account during our analysis. Most of the broadened reflections contain h or k indexes, and probably reveal the presence of stacking faults along *a* and *b* directions which correspond to the interlayer and the inter-chain directions, respectively (see schematic in *Figure 3*b).

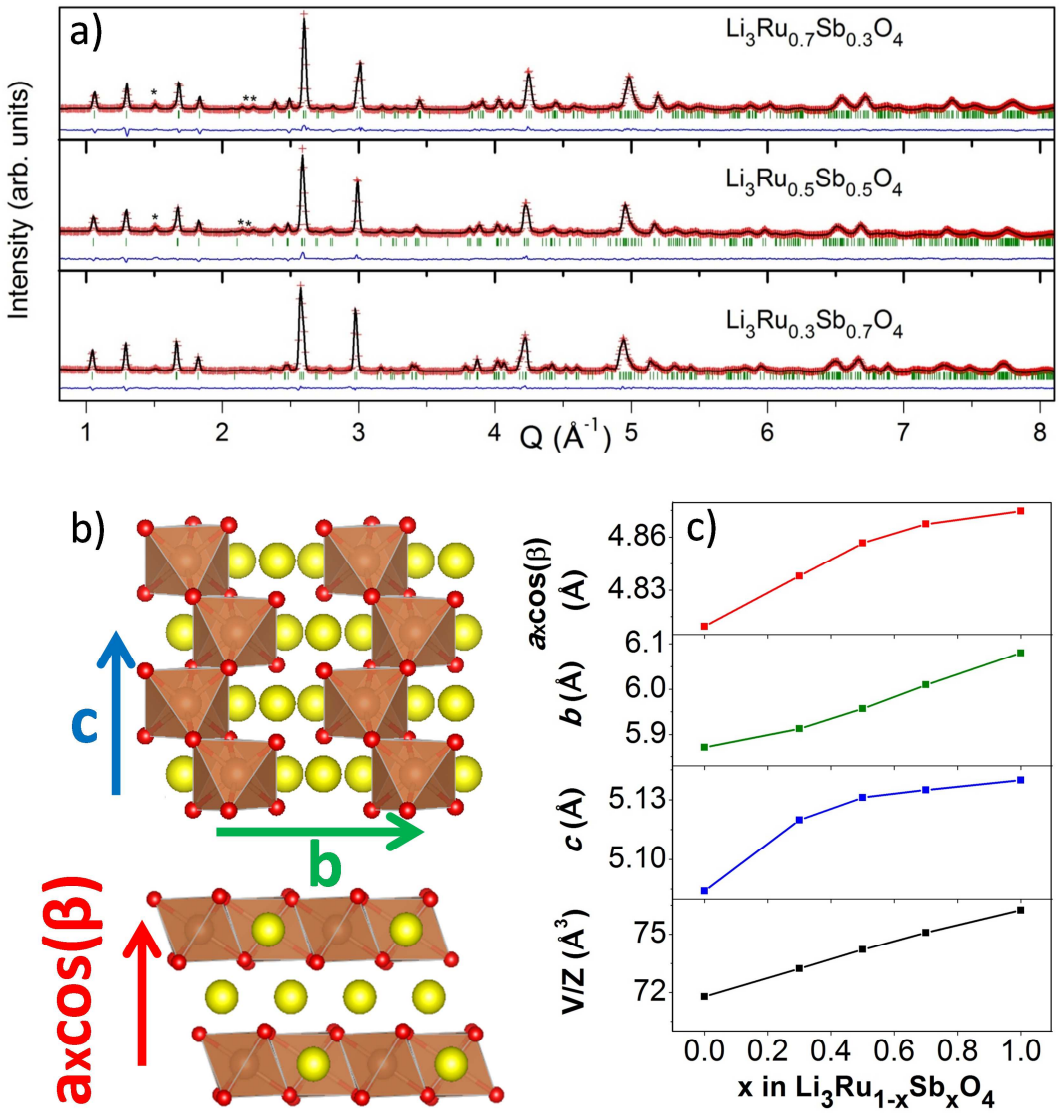

Figure 3

*a) Rietveld refinement of neutron diffraction patterns for $Li_3Ru_{0.7}Sb_{0.3}O_4$, $Li_3Ru_{0.5}Sb_{0.5}O_4$ and $Li_3Ru_{0.3}Sb_{0.7}O_4$ performed using the structural model of Li_3SbO_4 having a zig-zag chains structure. The red crosses, black continuous line and bottom blue line represent the observed, calculated, and difference patterns respectively. Vertical green tick bars are the Bragg positions. Li_2CO_3 was added as a secondary phase (marked with *). b) and c) Evolution of interlayer distance (axcos(β)), interchain distance b, c parameter and V/Z in red, green, blue, and black respectively along the solid solution together with two representations of the structure highlighting the reported distances. Error bars are included within the symbol size.*

We now focus on the $Li_3Sb_yNb_{1-y}O_4$ system (y = 0, 0.3, 0.5, 0.7, 1). By combining SXRD and NPD refinements and using the model of Li_3SbO_4, α–Li_3TaO_4, and β–Li_3TaO_4 for $Li_3Sb_{0.7}Nb_{0.3}$, $Li_3Sb_{0.5}Nb_{0.5}O_4$, and $Li_3Sb_{0.3}Nb_{0.7}O_4$, respectively, we could reliably refine all the intermediate structures, as can be seen in *Figure 4*) and Figure S2. Space group, cell parameters, and atomics positions are given in Tables 1), 2) and 3). For $Li_3Sb_{0.5}Nb_{0.5}O_4$ and $Li_3Sb_{0.3}Nb_{0.7}O_4$, we found that a partial disordering between Sb/Nb and Li greatly improves the fit. The same situation was observed for the $Li_3Ru_yNb_{1-y}O_4$ system for which electron microscopy didn't reveal Ru/Nb disorder. Actually, this disordering is an artificial way to tackle antiphase boundaries [31] which create local cooperative anti site defects, as explained in details in Ref 29.

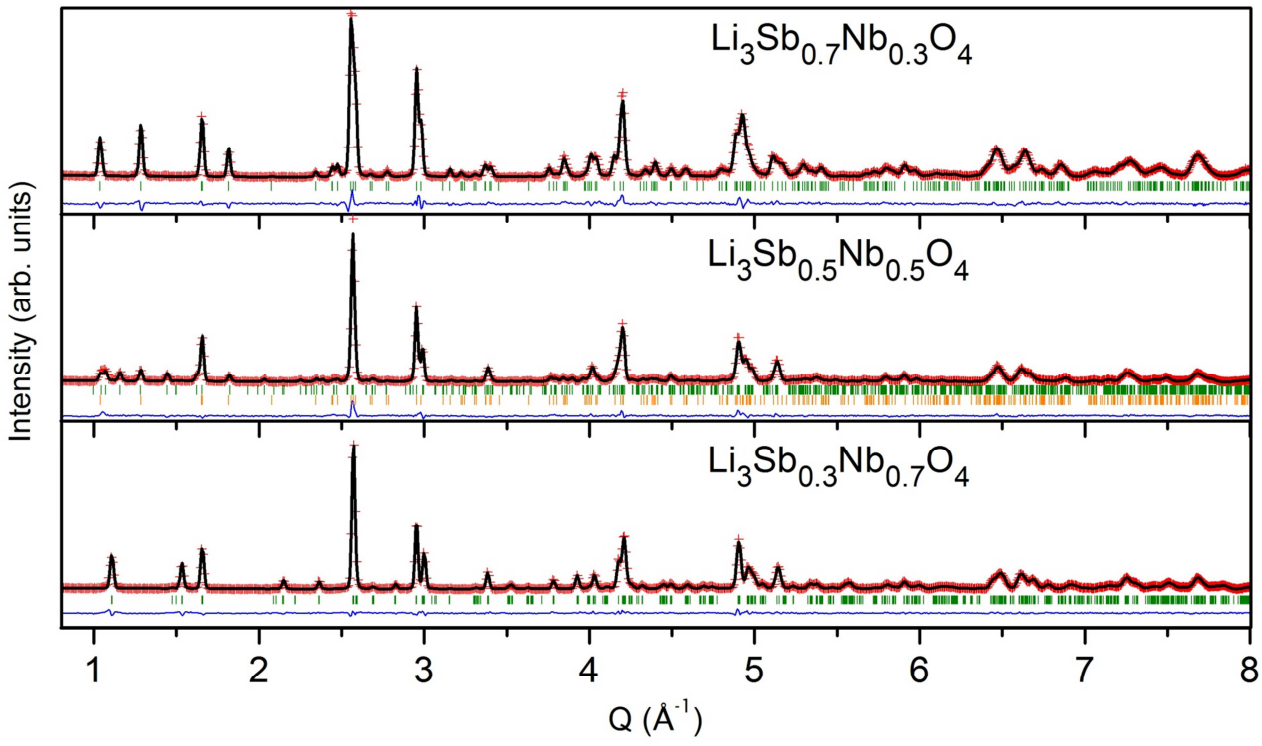

Figure 4

Rietveld refinement of neutron diffraction patterns for $Li_3Sb_{0.7}Nb_{0.3}O_4$, $Li_3Sb_{0.5}Nb_{0.5}O_4$ and $Li_3Sb_{0.3}Nb_{0.7}O_4$ performed with the structural model of Li_3RuO_4 (zig zag chains), α-Li_3TaO_4 and β-*Li_3TaO_4 (jagged chains), respectively. The red crosses, black continuous line and bottom blue line represent the observed, calculated, and difference patterns respectively. Vertical green tick bars are the Bragg positions. Second phase for $Li_3Sb_{0.5}Nb_{0.5}O_4$ pattern is fitted with $Li_3Sb_{0.7}Nb_{0.3}O_4$ model.*

Table 1): Crystallographic table for $Li_3Sb_{0.7}Nb_{0.3}O_4$ obtained by refinement of combined SXRD and NP patterns using the structural model of Li_3RuO_4 with $R_{bragg\ neutrons} = 3.51\%$. $R_{bragg\ SXRD} = 5.73\%$. $\chi^2_{neutrons} = 39.62$. $\chi^2_{SXRD} = 5.72$

$Li_3Sb_{0.7}Nb_{0.3}O_4$ zig – zag chains						
Space group *P* 2/*c*		Z = 2		V/Z = 76.258 Å^3		
a = 5.18099(6) Å, *b* = 6.05403(6) Å, *c* = 5.15324(5) Å and β = 109.338(7)°						
Atom	Wyckoff position	x	y	z	Biso (Å²)	occupancy
O1	4*g*	0.2234(6)	0.1059(4)	0.0013(7)	0.19(3)	1
O2	4*g*	-0.2467(6)	0.3612(4)	0.0237(6)	0.28(3)	1
Sb1/Nb1	2*e*	0	0.14751(19)	¼	0.41(9)	0.7/0.3
Li1	2*e*	0	0.618(2)	¼	1.12(8)	1
Li2	2*f*	½	0.133(3)	¼	1.12(8)	1
Li3	2*f*	½	0.4141(15)	¼	1.12(8)	1

Table 2): Crystallographic table for $Li_3Sb_{0.5}Nb_{0.5}O_4$ obtained by refinement of combined SXRD and NP patterns using the structural model of α – Li_3TaO_4 with $R_{bragg\ neutrons} = 1.63\%$. $R_{bragg\ SXRD} = 7.19\%$. $\chi^2_{neutrons} = 40.6$. $\chi^2_{SXRD} = 9.70$

$Li_3Sb_{0.5}Nb_{0.5}O_4$ α-Li_3TaO_4						
Space group *P* 2/*n*		Z = 6		V/Z = 76.06 Å^3		
a = 6.02691(4) Å, *b* = 6.00699(4) Å, *c* = 12.96630(10) Å and β = 103.533(5)°						
Atom	Wyckoff position	x	y	z	Biso	occupancy
O1	4*g*	0.0029(18)	0.1318(19)	0.2589(13)	0.78(4)	1
O2	4*g*	0.4901(18)	0.3776(18)	0.7460(13)	0.78(4)	1
O3	4*g*	0.1745(18)	0.3501(18)	0.0769(11)	0.78(4)	1
O4	4*g*	0.655(2)	0.359(2)	0.09307(11)	0.78(4)	1

O5	4*g*	0.6946(17)	0.112(2)	0.5888(11)	0.78(4)	1
O6	4*g*	0.148(2)	0.107(2)	0.5739(10)	0.78(4)	1
Sb1/Nb1/Li1	2*f*	1/4	0.600(6)	3/4	0.767(14)	0.40/0.40/0.2
Sb2/Nb2/Li2	4*g*	0.3938(3)	0.1231(4)	0.0828(2)	0.767(14)	0.45/0.45/0.1
Li3/Sb3/Nb3	2*e*	3/4	0.131(2)	3/4	0.91(9)	0.8/0.1/0.1
Li4/Sb4/Nb4	4*g*	0.451(2)	0.405(3)	0.5781(14)	0.91(9)	0.9/0.05/0.05
Li5	4*g*	-0.084(5)	0.117(6)	0.091(3)	0.91(9)	1
Li6	2*e*	1/4	0.361(8)	1/4	0.91(9)	1
Li7	2*f*	1/4	0.144(7)	3/4	0.91(9)	1
Li8	4*g*	0.601(5)	0.349(5)	-0.078(4)	0.91(9)	1

Table 3): Crystallographic table for $Li_3Sb_{0.3}Nb_{0.7}O_4$ obtained by refinement of combined SXRD and NP patterns using the structural model of β – Li_3TaO_4 *with* $R_{bragg\ neutrons} = 1.52\%$. $R_{bragg\ SXRD} = 16.68\%$. $\chi^2_{neutrons} = 39.9$. $\chi^2_{SXRD} = 1.86$.

$Li_3Sb_{0.3}Nb_{0.7}O_4$ jagged chains						
Space group *C* 2/*c* Z = 8 V/Z = 75.82 Å^3 *a* = 8.50754(6) Å, *b* = 8.51140(5) Å, *c* = 9.37868(7) Å and β = 116.7354(5)°						
Atom	Wyckoff position	x	y	z	Biso (Å²)	occupancy
O1	8*f*	0.1673(11)	-0.1256(10)	0.3615(10)	0.59(14)	1
O2	8*f*	0.9483(9)	-0.1070(8)	0.8887(9)	0.59(14)	1
O3	8*f*	0.4358(4)	-0.1378(6)	0.8840(9)	0.59(14)	1
O4	8*f*	0.6916(2)	-0.1295(8)	0.3670(7)	0.59(14)	1
Nb1/Sb1/Li1	8*f*	0.0775(2)	-0.1385(2)	0.1241(3)	0.486(16)	0.66/0.28/0.06
Li2	8*f*	0.326(3)	-0.108(3)	0.626(2)	1.27(4)	1
Li3/Nb2/Sb2	8*f*	0.543(2)	-0.123(2)	0.124(2)	1.27(4)	0.94/0.04/0.02
Li4	8*f*	0.827(3)	-0.119(3)	0.6433(19)	1.27(4)	1

Searching for an indicator that could explain the structural evolution, we plotted in *Figure 5* a), b) and d) the variations with the composition of three different structural parameters: the volume per formula unit (V/Z), the average M – O bond length, and the distortion coefficient of MO_6 written as Δ^{M-O}, respectively. The M – O distances grow upon going from Ru-rich, to Sb-rich, and to Nb-rich compounds. It is in agreement with the ionic radius of each element, i.e. 0.56 Å, 0.60 Å, and 0.64 Å for Ru^{5+}, Sb^{5+}, and Nb^{5+}, respectively. Interestingly, the cell volume doesn't follow this trend since it is the highest for Li_3SbO_4, despite an ionic radius smaller for Sb^{5+} than for Nb^{5+}. Also, the distortion coefficient stays roughly constant in the y Li_3RuO_4–(1-y)Li_3SbO_4 diagram while it grows as soon as Nb^{5+} is added to the composition. This trend mirrors the structural evolution, hence implying the importance of the structural distortion of the octahedra. It is worth mentioning that the distortion parameter deduced from diffraction analysis is averaged over the metallic atoms since they all share the same crystallographic site.

Since X-ray absorption spectroscopy is a site-sensitive and local technique, we can access directly the evolution of distortion around RuO_6, SbO_6, and NbO_6 in the different structures. The EXAFS oscillations extracted at Ru, Sb, and Nb K-edges contain information about the local environment around the absorbing atoms. The magnitude of the Fourier transform $|\chi(k)\, k^2|$ of the EXAFS oscillations (Figure 6, points) represents the atomic distribution around the Ru, Sb, and Nb atoms, where the first peak corresponds to the MO_6 octahedron (first shell). Fits for all compositions are reported as solid lines in *Figure 6* and the obtained results are summed up in Table S5. X-ray Absorption Near Edge Spectroscopy (XANES) are also presented in Figure S3. *Figure 5* c) and e) show the average M – O bond length and the distortion coefficient obtained by refining the 1st coordination shell around each metallic atom for all compositions. For a given atom, M – O distances and their associated distortion are almost constant over the phase diagram (Ru – O = 1.978(3) Å, Sb – O = 1.997(2) Å, and Nb – O = 2.025(5) Å; $\Delta RuO_6 = 33(1)\text{x}10^{-3}$, $\Delta SbO_6 = 23(1)\text{x}10^{-3}$, and $\Delta NbO_6 = 54(4)\text{x}10^{-3}$). Distortion of the MO_6 octahedra results from the displacement of the cations inside the octahedron, which will be called off-centering from here onward. The off-centering is triggered by the presence of two different oxygen atoms, O1 and O2, in the MO_6 octahedron, such that M tends to move towards the oxygen atom which is depleted in charge.[32] Off-centering is further increased, in the case of d^0 cations, by a second order Jahn-Teller effect. A second order Jahn-Teller effect is a structural distortion allowing the splitting of two quasi-

degenerated states, one filled and one empty, resulting in a lowering of the overall energy of the system. In the case of d^0 cations in octahedral configuration, the antibonding t_{2g} empty-states mix with the bonding t_{1u} filled-states breaking by the same the Oh symmetry through the displacement of metallic atom along the C4 or C3 axis of the octahedron. [33]

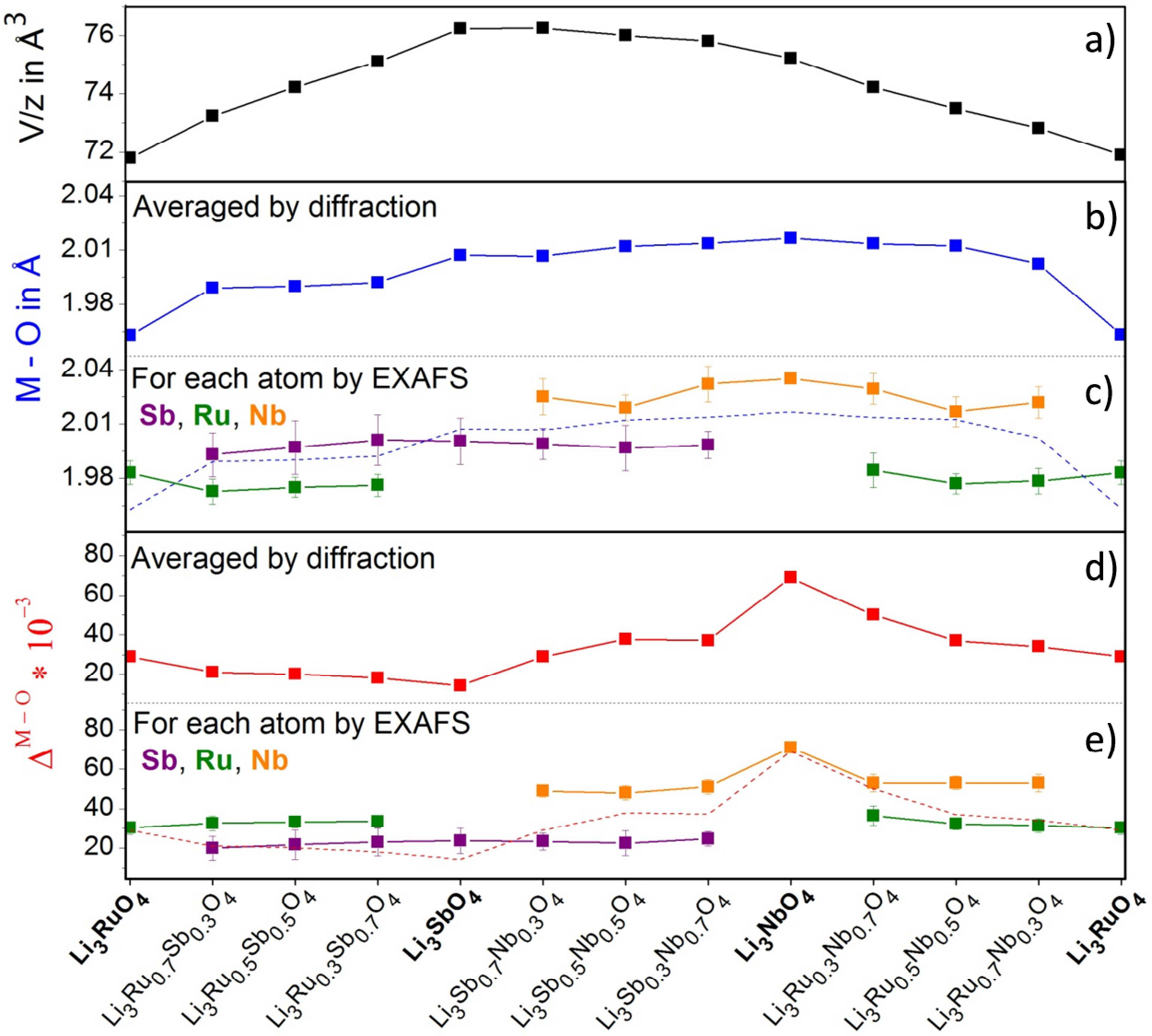

Figure 5: a) Volume/Z variation among the phase diagrams. b) and d) show the variation of the average M – O distance and distortion coefficient around the M atoms, respectively, as obtained by Rietveld refinement. c) and e) show the average M – O bond lenghts and distortion coefficient for each metallic atom (Ru in green, Nb in orange and Sb in purple), respectively, obtained by EXAFS analysis. Dashed line stand for the M – O and distortion coefficient obtained by Rietveld refinement. Distortion coefficient is calculated according the formula : $\Delta^{M-O} = \frac{1}{6}\sum_{i=1}^{6}\left[\frac{d_i - <d>}{<d>}\right]^2$

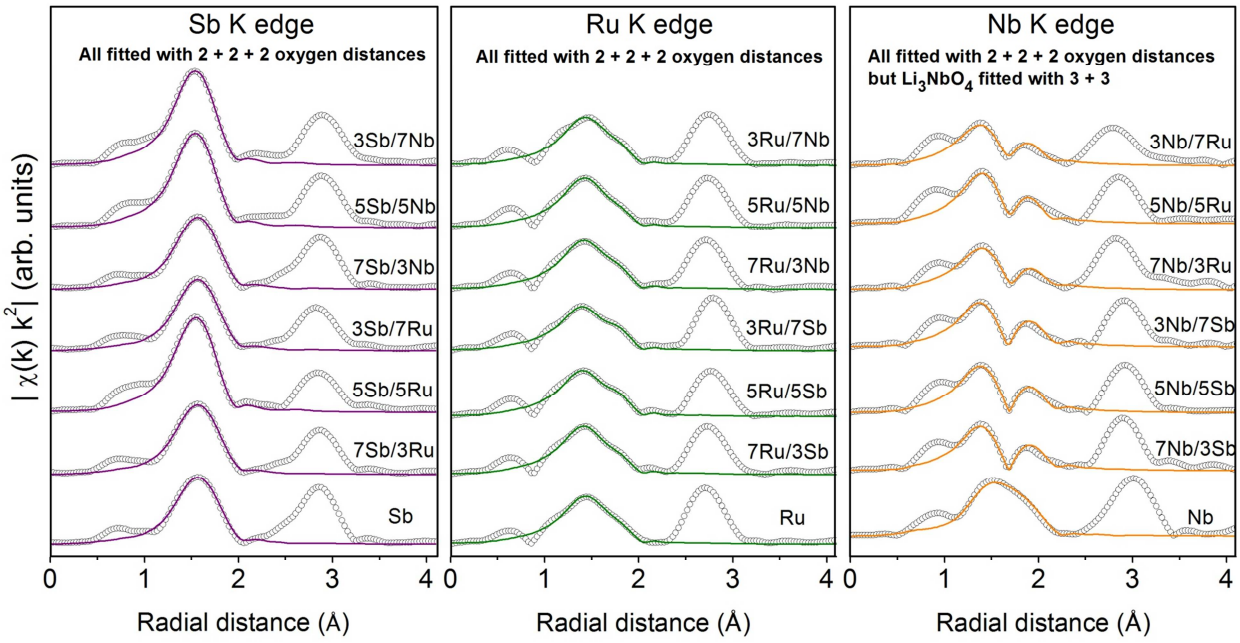

Figure 6: Magnitude of the Fourier transforms of the EXAFS oscillations extracted at the Sb K-edge, Ru K-edge, and Nb K-edge for the left, middle and right panel respectively. The solid lines represent the model fitting for the M-O shell.

The structures of the three binary systems: y Li_3RuO_4–(1-y) Li_3NbO_4, y Li_3RuO_4–(1-y) Li_3SbO_4, and y Li_3SbO_4–(1-y) Li_3NbO_4 for y = 1, 0.7, 0.5, 0.3, and 0 have been thoroughly examined, and they can now be used as inputs for first-principles DFT calculations in order to rationalize the observed structural evolution. The open questions are: i) Is cationic disordering between Ru, Nb, and Sb stabilized thermodynamically? and ii) can the structural evolution be rationalized by a simple parameter?

Concerning cationic disordering, DFT calculations were used to estimate the energy differences between several ordered configurations for $Li_3Ru_{0.5}Nb_{0.5}O_4$, $Li_3Ru_{0.5}Sb_{0.5}O_4$, and $Li_3Nb_{0.5}Sb_{0.5}O_4$. The results are presented in *Figure 7*. For $Li_3Ru_{0.5}Sb_{0.5}O_4$, the energy differences between monomers (e.g. all Ru are bonded to Sb and so are the Sb to the Ru), dimers, and chains are around 14 meV/F.U. None of these configurations significantly lowers the enthalpy, which suggests that cationic disordering stabilized by entropy might be the most stable system. Turning to $Li_3Ru_{0.5}Nb_{0.5}O_4$, energy of structures containing Nb clusters forming dimers (ground state) or trimers (7 meV above the ground state) are the lowest among the tested configurations. In the case of $Li_3Nb_{0.5}Sb_{0.5}O_4$, structures showing the lowest energies present chains of Nb or Sb (ground state) and clusters of 6 units of Nb and Sb (4 meV above the ground state). The study of these two compositions suggests that for compounds containing Nb, transition metal clustering is more likely

to happen. However, it will still not lead to long-range ordering since different clusters can be present in a disordered fashion. Overall, whatever the phases described herein, energy calculations suggest that the described structures are most likely stabilized by disordering, with however a local ordering in the case of niobium.

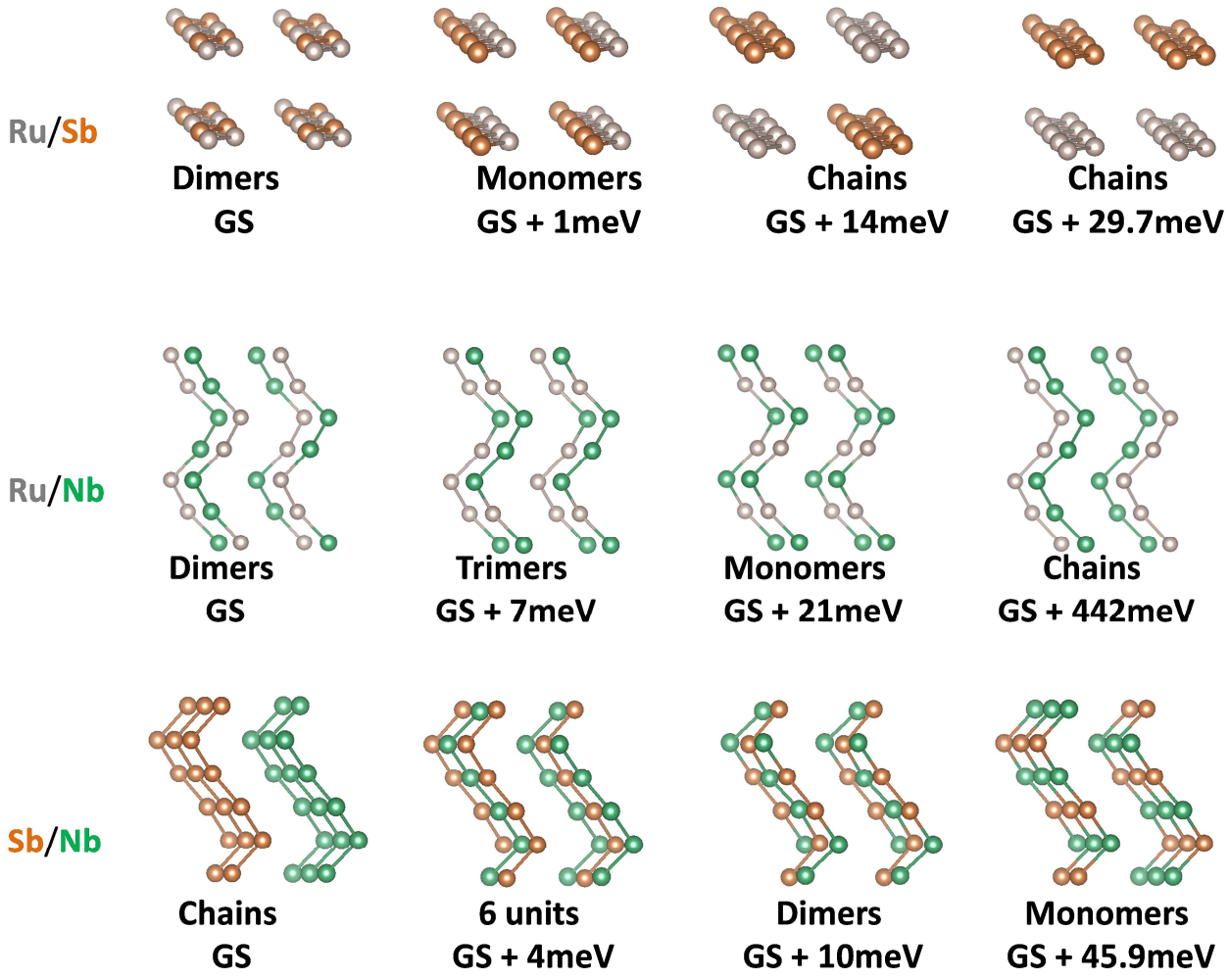

Figure 7

Metallic framework of $Li_3Ru_{0.5}Sb_{0.5}O_4$, $Li_3Ru_{0.5}Nb_{0.5}O_4$ and $Li_3Sb_{0.5}Nb_{0.5}O_4$ with specific Ru/Nb, Ru/Sb and Sb/Nb orderings, in the top, middle and bottom part, respectively together with the difference in energy per formula unit with the ground state (GS). For sake of clarity only the M (M = Ru, Nb and Sb) atoms are represented and bonds are drawn between them.

Next we tried to identify a simple indicator that could explain the obtained structural evolution. Amongst the ones considered, three retained our attention: 1) electrostatic interactions, 2) the presence of a d^0 element, and 3) the off-centering of M in the MO_6 octahedron.

Owing to the high electronegativity of oxygen, many oxide structures possess strongly ionic bonds and, therefore, their structural packing can be explained by simple electrostatic effects.

Pursuing this direction, structural models for Li_3RuO_4, Li_3SbO_4, and Li_3NbO_4 with different structures were obtained by relaxing the ions through DFT. Then, Madelung electrostatic energies were calculated using formal charges and Bader charges, as presented in *Figure 8*-a). Among the three systems explored, the zig-zag-chains structure, which turns out to be the one experimentally adopted by Li_3SbO_4 and Li_3RuO_4, is the most stable in terms of minimizing electrostatic interactions. However, Li_3NbO_4 escapes this logic since it does not crystallize in the zig-zag chains structure. To see if the ground state for Li_3NbO_4 can be retrieved using a more sophisticated model, DFT energy calculations were considered and presented *Figure 8* –a). With DFT, the most stable structure for Li_3NbO_4 is the clusters structure, in agreement with experiments. Applying this methodology to Li_3RuO_4, one can notice that all the different structures, i.e. zig-zag chains, helical chains, α–Li_3TaO_4 chains, and jagged chains, are very close in energy (less than 14 meV). This indicates that Li_3RuO_4 could be obtained in a disordered rocksalt structure as well. This is in agreement with our experimental data since this compound can indeed be synthetized partially disordered (*Figure 8*-b) via short annealing times at 700°C. Interestingly, Li_3SbO_4 cannot be synthetized in a disordered rocksalt structure [16]. Such a difference might be due to the higher ionicity of the Sb – O bond compared to the Ru – O bond, which enhances the importance of electrostatic interactions to the phase stability, hence stabilizing the zig-zag-chains structure for Li_3SbO_4. Overall, electrostatic energy considerations can explain the structure for Li_3RuO_4 and Li_3SbO_4, but fail for Li_3NbO_4. This might be nested in the d^0 configuration of Nb^{5+} in Li_3NbO_4, as discussed next.

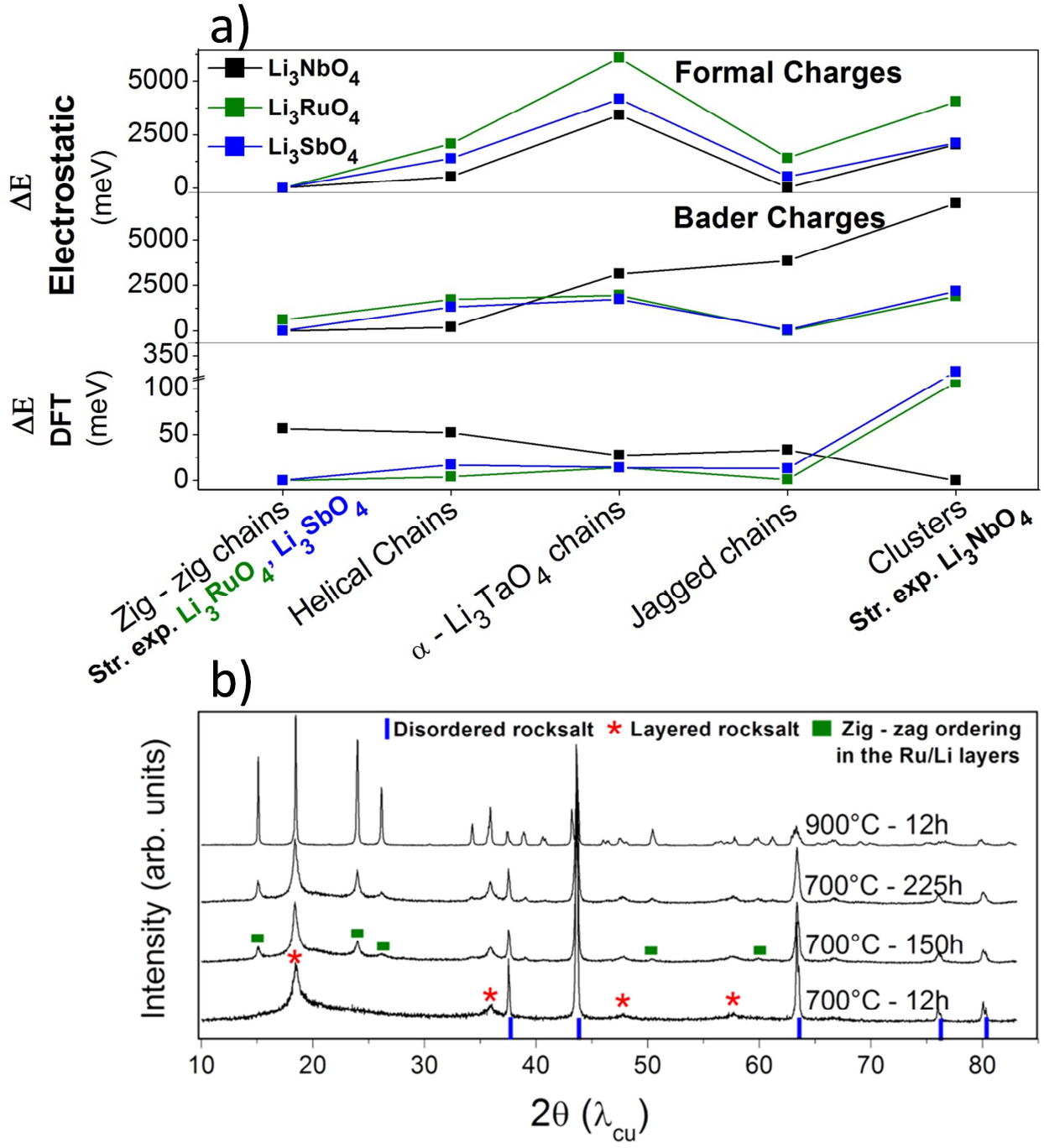

Figure 8

a) Difference of electrostatic energies (ΔE electrostatics) calculated using formal charges, Bader charges and DFT energies (ΔE DFT) with the ground state for Li_3NbO_4, Li_3RuO_4 and Li_3SbO_4 in the different structures obtained in the $Li_3(Ru,Nb,Sb)O_4$ binary system. b) XRD patterns of Li_3RuO_4 synthetized at different temperatures and for different times. When synthetized at 700°C – 12h, it crystallizes in a disordered rocksalt structure with a partial layered ordering between the Ru and Li, then going at higher temperature or longer time, the superstructure peaks corresponding to the Ru/Li ordering inside the Ru/Li layers appear.

While exploring the Nb-based binary phases (*Figure 2*), one can observe that the addition of Nb rapidly triggers structural transitions, suggesting an eventual effect of having an empty d shell (d^0-metal). To further probe this hypothesis, we embarked into a comparison with another d^0 element, Ta^{5+}. Li_3TaO_4 crystallizes in two polymorphs: α-Li_3TaO_4 which is isostructural to $Li_3Sb_{0.5}Nb_{0.5}O_4$ or $Li_3Ru_{0.3}Nb_{0.7}O_4$, and β-Li_3TaO_4 which possesses a structure alike $Li_3Sb_{0.3}Nb_{0.7}O_4$. Both structures are not stable ones considering electrostatic interactions only. Thus we synthetized $Li_3Ru_{0.5}Ta_{0.5}O_4$, whose XRD pattern and Rietveld refinement can be seen in the Supporting Information Figure S4. It crystallizes in the same structure as $Li_3Ru_{0.5}Nb_{0.5}O_4$, which is different from the d^0-free $Li_3Ru_{0.5}Sb_{0.5}O_4$, supporting the fact that there might be a correlation between structure and d-metals having empty d shells (d^0). This was an impetus to look for a property of d^0 elements that could explain the structural evolution.

Within this context, we should recall that d^0 compounds are prone to second order Jahn-Teller effect which is associated to a distortion that displaces the M from the center of the MO_6 octahedron. Interestingly, we have seen from the structural analysis that the distortion coefficient values follow the structural evolution. All together, these two effects point towards the importance such a distortion could have on the structural evolution. We explored the effect of the distortion in zig-zag chains and clusters structures on the oxygen charges. For this, a set of structures with different cation off-centerings was constructed and distortion coefficients and Bader charges were calculated. We found that the metal off-centering changes the charge distribution among the oxygen atoms of the MO_6 octahedron. In the specific case of Li_3MO_4 structures, two different types of oxygen atoms, labelled O1 and O2, are present, with the displacement of M being always shifted towards O1. This translates into the increase of the charge in O1 by δ_{O1} and a decrease in the charge of O2 by δ_{O2} as illustrated in *Figure 9*-a (δ_{O1} being negative since the oxygen charge is negative and δ_{O2} positive for the same reason). Moreover, the difference between δ_{O2} and δ_{O1} increases when the distortion gets more severe (right panel of *Figure 9*-a). To evaluate the charge difference for a specific composition of metals, we determine the off-centering parameter associated to each of the Sb^{5+}, Nb^{5+}, Ta^{5+}, and Ru^{5+} ions. For this, zig-zag, helical, α–Li_3TaO_4, jagged chains, and clusters structures for Li_3SbO_4, Li_3RuO_4, Li_3TaO_4, and Li_3NbO_4 were relaxed by DFT, and the resulting distortion coefficients are shown in *Figure 9* – b). We could demonstrate that each cation presents distinct off-centerings associated to the distortion coefficient values of 23 x 10^{-3}, 33 x 10^{-3}, 45 x 10^{-3}, and 54 x 10^{-3} for Sb^{5+}, Ru^{5+}, Ta^{5+}, and Nb^{5+}, respectively. It is worth mentioning that

these values are in agreement with those experimentally obtained. As the difference in charge (δ_{O2} - δ_{O1}) scales with the distortion coefficient (right panel of *Figure 9*-a), δ_{O2} - δ_{O1} will be higher in NbO_6, than in TaO_6, RuO_6, and finally SbO_6. Obviously, when considering the overall structure, these MO_6 octahedra will try to order so that their specific charge distribution is stabilized. An adequate way to estimate this stabilization is to compare the difference between the O1 and O2 Madelung site potentials for each structure. O site potentials and their difference have been calculated for the zig-zag, helical, α–Li_3TaO_4, jagged chains and clusters structure for Li_3RuO_4, Li_3SbO_4, Li_3TaO_4 and Li_3NbO_4. The average values obtained among the four compositions are shown in *Figure 9*-c. From this figure, one can see that the difference is the largest for the clusters structure, then for the jagged, α–Li_3TaO_4, zig-zag, and finally the helical chains structures. This suggests that clusters structure, which shows the largest O site potentials difference, should stabilize highly distorted NbO_6 octahedra (having the largest difference δ_{O2} - δ_{O1}). Note that this is in agreement with the crystallization of Li_3NbO_4 in a clusters structure. Following this reasoning, α–Li_3TaO_4 and jagged chains structures should stabilize TaO_6 octahedra, which is once again the case. Finally, Li_3SbO_6 and Li_3RuO_4 crystallize in the zig-zag chain, because Ru^{5+} and Sb^{5+} induce a weak charge density difference between O1 and O2.

Overall, we have demonstrated that Li_3SbO_4 and Li_3RuO_4 crystallize in the zig-zag chain because it minimizes the electrostatic interactions. However for compounds having d^0 metals (Li_3TaO_4 and Li_3NbO_4), such electrostatic interactions are overruled by the second order Jahn-Teller effect which is accompanied by displacement of the cations out of the octahedron center. While Li_3NbO_4 crystallizes in the clusters structure, Li_3TaO_4 forms in the α–Li_3TaO_4 structure or in the jagged chains structures due to lower displacement values for Ta^{5+} compared to Nb^{5+}.[34] For $Li_3M_yM'_{1-y}O_4$ (M and M' being Ru, Sb, Ta or Nb), the average distortion coefficient Δ^{M-O} can be used to predict the structure: for Δ^{M-O} varying between 20 x 10^{-3} and 30 x 10^{-3}, zig-zag chains will be preferred, while helical and jagged chains have a greater chance to be found for Δ^{M-O} ranging from 37.5.10^{-3} to 42.10^{-3} and 43.10^{-3} to 48.10^{-3}, respectively. Beyond these values, clusters structure is more likely to be formed.

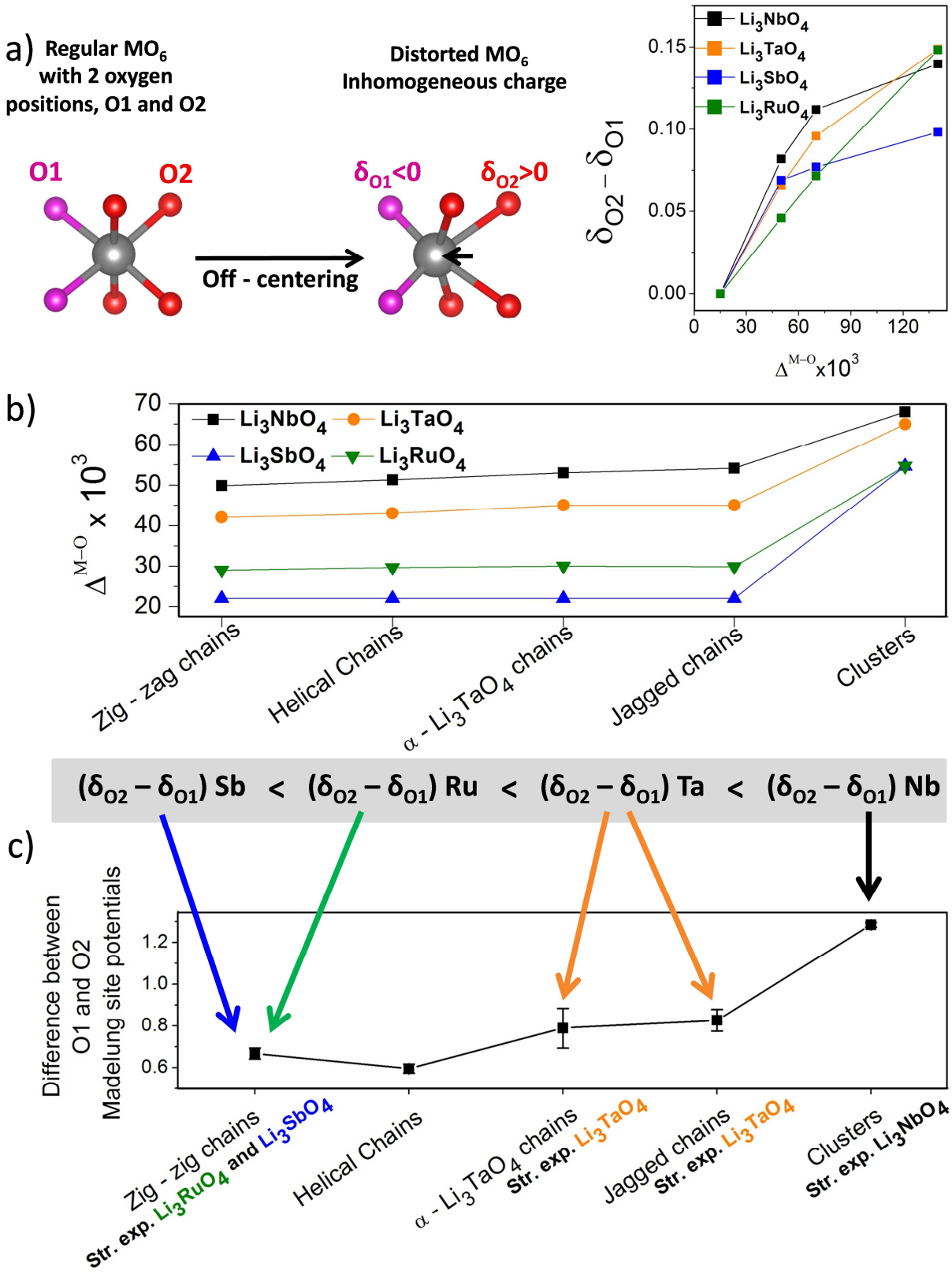

Figure 9

a) Schematic of the charge distribution evolution in the MO_6 octahedron with the displacement of the M atoms (M = Ru, Nb, Sb or Ta), together with the evolution of the Bader charge difference $\delta_{O2} - \delta_{O1}$ with the amplitude of the distortion, δ_{O2} and δ_{O1} being the charge lost by O2 and gained by O1, respectively. Charges were calculated for Li_3NbO_4,

Li_3RuO_4, Li_3SbO_4, and Li_3TaO_4 in the zig –zag structure with different displacement values. b) Distortion coefficient Δ^{M-O} obtained from Li_3NbO_4, Li_3RuO_4, Li_3SbO_4 and Li_3TaO_4 converged through DFT in the zig-zag chains, helical chains, α–Li_3TaO_4, jagged chains and clusters structures. The obtained values match with the experimental values obtained for Nb^{5+}, Ru^{5+} and Sb^{5+}. c) average difference Madelung site potentials between O1 and O2 calculated for undistorted zig-zag chains, helical chains, α–Li_3TaO_4, jagged chains and clusters structures for Li_3NbO_4, Li_3RuO_4, Li_3SbO_4 and Li_3TaO_4.

Conclusions

In this study, we have unveiled the rich crystal chemistry of the $Li_3Ru_ySb_{1-y}O_4$ and $Li_3Sb_yNb_{1-y}O_4$ systems and rationalized the structural evolution as a function of y. Through combined synchrotron and neutron powder diffraction studies, we have showed that $Li_3Ru_ySb_{1-y}O_4$ is a solid-solution system while $Li_3Sb_yNb_{1-y}O_4$ has a complex phase diagram with well-defined intermediate phases for y = 0.3, 0.5, and 0.7. Nevertheless, all compositions form rocksalt structures with different Li/M orderings (M being Ru, Sb, or Nb) leading to different metallic frameworks with no sign of ordering between Ru, Sb and Nb. Through X-ray Absorption Spectroscopy (XAS) and the exploitation of the EXAFS oscillations collected at the Ru, Sb, and Nb K-edges, we could show that all M keep their MO_6 geometry, M-O bond length, and distortion coefficient in the whole range of compositions. DFT calculations were used to assess the relative energies of various cation orderings and to establish a reliable indicator capable of explaining the structural evolution through M,M' substitutions. It is confirmed that cation disordering is thermodynamically stable and that the structural evolution arises from a delicate balance between electrostatic interactions and second-order Jahn-Teller effect. While electrostatic interactions allow rationalizing the structures for Li_3RuO_4, Li_3SbO_4, and their mixed $Li_3Ru_ySb_{1-y}O_4$ compositions, the second-order Jahn-Teller effect is responsible for the structural change when a d^0 cation is added to the structure. This distortion induces an inhomogeneous charge repartition among the oxygen atoms of the MO_6 octahedron modifying by the same the long-range ordering of cations to compensate this not uniform charge distribution on the oxygen network. Such finding regarding the delicate balance between electrostatic and second-order Jahn-Teller effects is of great importance for designing new electrode materials or ionic conductors, bearing in mind that such structural issues strongly influence ion transport. Prior to encouraging other researchers to explore further this road, we must also emphasize that this delicate balance is also affected by the nature of the alkali metal. For instance, irrespective of the d-metal, Na_3RuO_4, Na_3NbO_4, and Na_3TaO_4 were reported to crystallize

in the same structure, in which the metallic framework forms plaquettes of 4 metal centers. Such a phase does not exist among the Li_3MO_4 phases, hence showing the complexity and the subtlety of structural stability within the A_3MO_4 family. Such materials are being tested for their electrochemical properties vs. Li^+ so as to identify the key structural features for achieving optimized electrochemical performances together with their stability with respect to O_2 release upon Li removal.

Acknowledgments:

The authors thank Vivian Nassif for her help in neutron diffraction experiment at the D1B diffractometer at ILL. The authors also thank V. Briois and S. Belin for helpful discussions on XAS analysis and synchrotron SOLEIL (France) for providing beamtime at the ROCK beamline (financed by the French National Research Agency (ANR) as a part of the "Investissements d'Avenir" program, reference: ANR-10-EQPX-45; proposal #20160095). Use of the Advanced Photon Source at Argonne National Laboratory was supported by the U. S. Department of Energy, Office of Science, Office of Basic Energy Sciences, under Contract No. DE-AC02-06CH11357. Q. J. thanks the ANR “Deli-Redox” for PhD funding. J.-M.T. acknowledges funding from the European Research Council (ERC) (FP/2014)/ERC Grant-Project 670116-ARPEMA.

Author information:

Corresponding author: jean-marie.tarascon@college-de-france.fr

Author Contribution:

Q.J. designed the research approach and carried out the synthesis, Q.J. and G.R. did the diffraction experiments and analysis, Q.J. and A.I. conducted the XAS measurements and analysis, Q.J., M.S. and M.-L.D. performed the DFT study, Q.J., G.R. and J.M.T. wrote the manuscript, and all authors discussed the experiments and edited the manuscript.

Supporting information:

Crystallographic data, additional Rietveld refinements, EXAFS analysis.

References:

(1) Takayama, T.; Kato, A.; Dinnebier, R.; Nuss, J.; Kono, H.; Veiga, L. S. I.; Fabbris, G.; Haskel, D.; Takagi, H., Hyperhoneycomb Iridate β − Li 2 IrO 3 as a Platform for Kitaev Magnetism, *Phys. Rev. Lett*. **2015**, *114, 077202*.

(2) Prasad, B. E.; Kazin, P.; Komarek, A. C.; Felser, C.; Jansen, M.; β-Ag_3RuO_4, a Ruthenate(V) Featuring Spin Tetramers on a Two-Dimensional Trigonal Lattice, *Angew. Chem. Int. Ed.* **2016**, *55*, 4467–4471.

(3) Ma, J.-L.; Fu, Z.-F.; Liu, P.; Wang, B.; Li, Y., Microwave dielectric properties of low-fired Li_2TiO_3–MgO ceramics for LTCC applications, *Mater. Sci. Eng. B* **2016**, *204*, 15–19.

(4) Zhou, H.; Wang, W.; Chen, X.; Miao, Y.; Liu, X.; Fang, L.; He, F., Sintering behavior, phase evolution and microwave dielectric properties of thermally stable (1−x)Li_3NbO_4−x$CaTiO_3$ composite ceramic, *Ceram. Int.* **2014**, *40*, 2103–2107.

(5) Mizushima, K.; Jones, P. C.; Wiseman, P. J.; Goodenough J. B.;, Li_xCoO_2 (0< x<-1): A new cathode material for batteries of high energy density, *Mater. Res. Bull.* **1980**, *15*, 783–789.

(6) Komaba, S.; Yabuuchi, N.; Nakayama, T.; Ogata, A.; Ishikawa, T.; Nakai, I.; Study on the Reversible Electrode Reaction of $Na_{1-x}Ni_{0.5}Mn_{0.5}O_2$ for a Rechargeable Sodium-Ion Battery, *Inorg. Chem.* **2012**, *51*, 6211–6220.

(7) Hoppe, E.; Stewner, F.; Notiz über das System LilnO2/LiNiO2, ZAAC **1971**, 380, 244-249.

(8) Mather, G. C.; Dussarrat, C.; Etourneau, J.; West, A. R.; A review of cation-ordered rock salt superstructure oxides, *J. Mater. Chem.* **2000**, *10*, 2219–2230.

(9) Fletcher, J. G.; Mather, G. C.; West, A. R.; Castellanos, M.; Gutierrez, M. P.; Li 3 Ni 2 TaO 6: A novel rock salt superstructure phase with partial cation order*, J. Mater. Chem.* **1994**, *4*, 1303–1305.

(10) McCalla, E.; Abakumov, A.; Rousse, G.; Reynaud, M.; Sougrati, M. T.; Budic, B.; Mahmoud, A.; Dominko, R.; Van Tendeloo, G.; Hermann, R. P.; Tarascon, J.-M.; Novel Complex Stacking of Fully-Ordered Transition Metal Layers in Li_4FeSbO_6 Materials , *Chem. Mater.* **2015**, *27*, 1699–1708.

(11) Pauling L., The principles determining the structure of complex ionic crystals, *J. Am. Chem. Soc.* **1929**, *51*, 1010–1026.

(12) Brunel, M.; De Bergevin, F.; Gondrand, M.; Determination theorique et domaines d'existence des differentes surstructures dans les composes A^{3+} B^{1+} $X2^{2-}$ de type NaCl , *J. Phys. Chem. Solids* **1972**, *33*, 1927–1941.

(13) Hauck, J.; Short-Range Order and Superstructures of Ternary Oxides AMO_2, A_2MO_3 and A_5MO_6 of Monovalent A and Multivalent M Metals Related to the NaCl Structure, *Acta Cryst.* 1980, A36, 228–237.

(14) Ukei, K.; Suzuki, H.; Shishido, T.; Fukuda, T.; Li_3NbO_4, *Acta Crystallogr.* **1994**, *50*, 655–656.

(15) Du Boulay, D.; Sakaguchi, A.; Suda, K.; Ishizawa, N.; Reinvestigation of β-Li_3TaO_4, *Acta Crystallogr. Sect. E* **2003**, *59*, i80–i82.

(16) Skakle, J. M.; Tovar, S. T.; Fray, S. M.; West, A. R.; The crystal structure of Li_3SbO_4, *J. Mater. Chem.* **1996**, *6*, 1939–1942.

(17) Yabuuchi, N.; Takeuchi, M.; Nakayama, M.; Shiiba, H.; Ogawa, M.; Nakayama, K.; Ohta, T.; Endo, D.; Ozaki, T.; Inamasu, T.; Sato, K.; Komaba, S.; High-capacity electrode materials for rechargeable lithium batteries: Li_3NbO_4 -based system with cation-disordered rocksalt structure, *Proc. Natl. Acad. Sci.* **2015**, *112*, 7650–7655.

(18) Perez, A. J.; Jacquet, Q.; Batuk, D.; Iadecola, A.; Saubanère, M.; Rousse, G.; Larcher, D.; Vezin, H.; Doublet, M.-L.; Tarascon, J.-M.; *accepted Nat. Energy*. 2017.

(19) Pearson, R. G.; The second-order Jahn-Teller effect , *J. Mol. Struct. THEOCHEM* **1983**, *103*, 25–34.

(20) Rodríguez-Carvajal, J.; Recent advances in magnetic structure determination by neutron powder diffraction, *Phys. B Condens. Matter* **1993**, *192*, 55–69.

(21) Briois, V.; La Fontaine, C.; Belin, S.; Barthe, L.; Moreno, T.; Pinty, V.; Carcy, A.; Girardot, R.; Fonda, E.; ROCK: the new Quick-EXAFS beamline at SOLEIL, *J. Phys. Conf. Ser.* **2016**, *712*, 012149.

(22) Ravel, B.; Newville, M.; ATHENA, ARTEMIS, HEPHAESTUS: data analysis for X-ray absorption spectroscopy using IFEFFIT, *J. Synchrotron Radiat.* **2005**, *12*, 537–541.

(23) Kresse, G.; Hafner, J.; Ab Initio molecular dynamics for liquid metals, *Physical Review B*. 1993, 558.

(24) Kresse, G.; Furthmüller, J.; Efficiency of ab-initio total energy calculations for metals and semiconductors using a plane-wave basis set, *Computational Materials Science*. 6th ed. 1996, 15–50.

(25) Perdew, J. P.; Burke, K.; Ernzerhof, M.; Generalized Gradient Approximation Made Simple, *Phys. Rev. Lett.* **1996**, *77*, 3865–3868.

(26) Dudarev, S. L.; Botton, G. A.; Savrasov, S. Y.; Humphreys, C. J.; Sutton, A. P.; Electron-energy-loss spectra and the structural stability of nickel oxide: An LSDA+ U study, *Phys. Rev. B* **1998**, *57*, 1505.

(27) Manuel, P.; Adroja, D. T.; Lindgard, P.-A.; Hillier, A. D.; Battle, P. D.; Son, W.-J.; Whangbo, M.-H.; Neutron scattering and μ SR investigations of quasi-one-dimensional magnetism in the spin = 3 / 2 compound Li 3 RuO 4, *Phys. Rev. B* **2011**, *84*, 174430.

(28) Son, W.-J.; Manuel, P.; Adroja, D.; Whangbo, M.-H.; Density Functional Analysis of the Magnetic Structure of Li_3RuO_4: Importance of the Ru–O···O–Ru Spin-Exchange Interactions and Substitutional Ru Defects at the Li Sites, *Inorg. Chem.* **2011**, *50*, 9400–9405.

(29) Jacquet, Q.; Perez, A.; Batuk, D.; Van Tendeloo, G.; Rousse, G.; Tarascon, J.-M.; The $Li_3Ru_yNb_{1-y}O_4$ ($0 \le y \le 1$) System: Structural Diversity and Li Insertion and Extraction Capabilities, *Chem. Mater.* **2017**, *29*, 5331–5343.

(30) Zocchi, M.; Gatti, M.; Santoro, A.; Roth, R. S.; Neutron and X-ray diffraction study on polymorphism in lithium orthotantalate, Li_3TaO_4, *J. Solid State Chem.* **1983**, *48*, 420–430.

(31) Casas-Cabanas, M.; Kim, C.; Rodríguez-Carvajal, J.; Cabana, J.; Atomic defects during ordering transitions in $LiNi_{0.5}Mn_{1.5}O_4$ and their relationship with electrochemical properties, *J Mater Chem A* **2016**, *4*, 8255–8262.

(32) Kunz, M.; David Brown, I. Out-of-center Distortions around Octahedrally Coordinated d0 Transition Metals, *J. Solid State Chem.* **1995**, 115, 395–406.

(33) Halasyamani, P. S.; Asymmetric Cation Coordination in Oxide Materials: Influence of Lone-Pair Cations on the Intra-octahedral Distortion in d^0 Transition Metals, *Chem. Mater.* **2004**, *16*, 3586–3592.

(34) Ok, K. M.; Halasyamani, P. S.; Casanova, D.; Llunell, M.; Alemany, P.; Alvarez, S. Distortions in Octahedrally Coordinated d^0 Transition Metal Oxides: A Continuous Symmetry Measures Approach, *Chem. Mater.* **2006**, *18*, 3176–3183.

TOC :

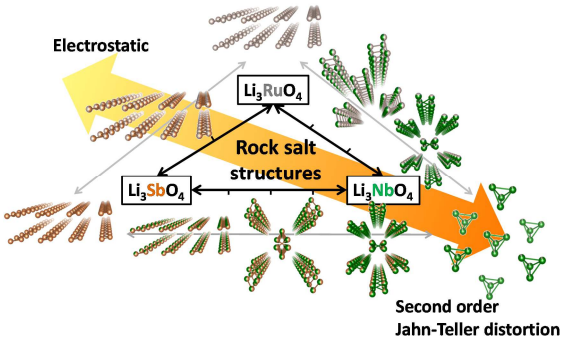
Electrostatic
Li_3RuO_4
Rock salt
structures
Li_3SbO_4
Li_3NbO_4
Second order
Jahn-Teller distortion